

Cell Reports, Volume 42

Supplemental information

**Global and tissue-specific
aging effects on murine proteomes**

Gregory R. Keele, Ji-Gang Zhang, John Szpyt, Ron Korstanje, Steven P. Gygi, Gary A. Churchill, and Devin K. Schweppe

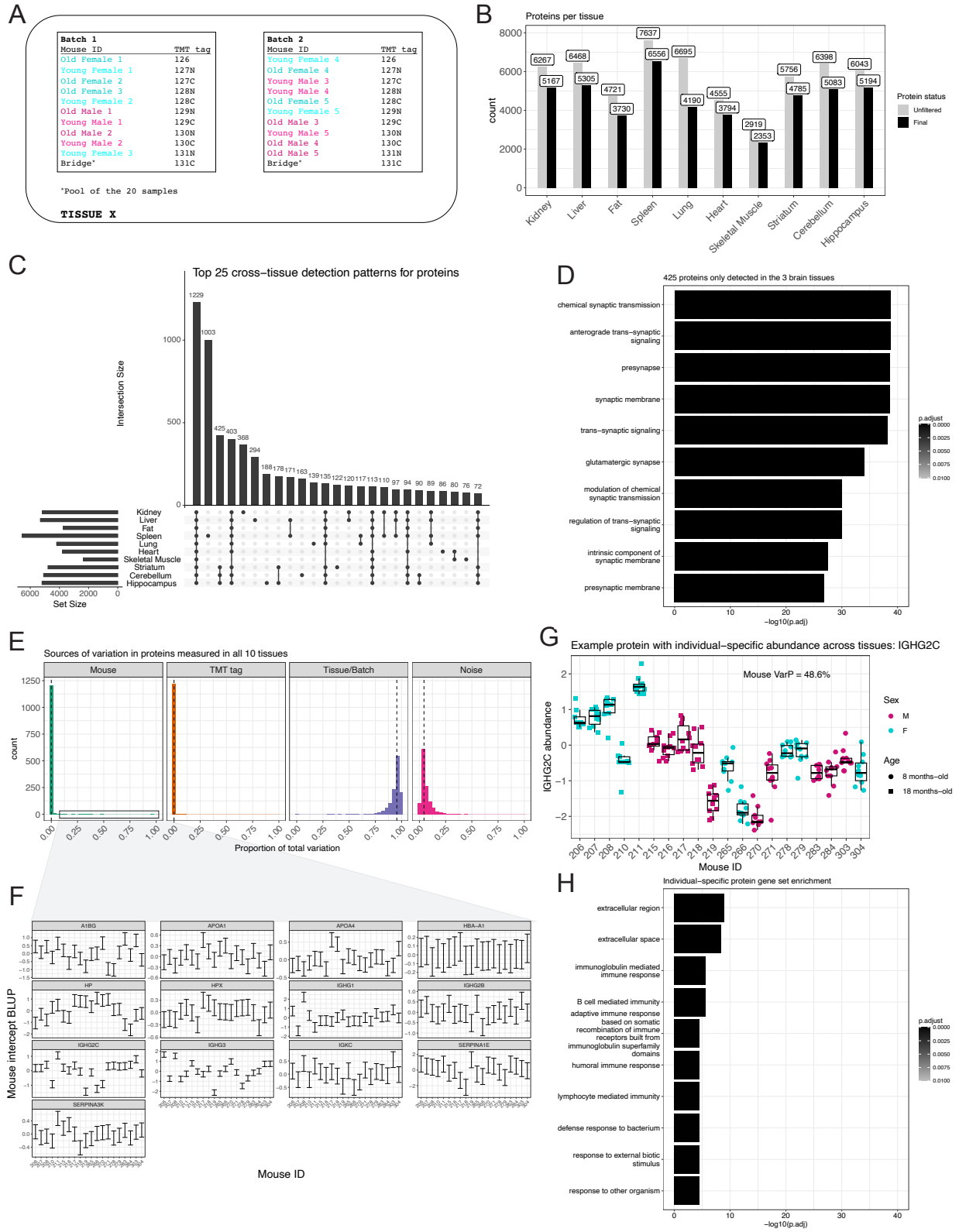


Figure S1. Summaries of the proteomics experiment and proteins with individual-specific abundance across 10 tissues.

- (A) Diagram of the TMT plex design used for 10 tissues, matching mouse IDs (sex and age group) to TMT tags. The bridge sample represents a pooled sample of all 20 mice included across all plexes.
- (B) The total number of proteins quantified and analyzed after filtering out proteins detected in only a single batch for a given tissue.
- (C) The number of proteins that were detected and analyzed for specific sets of tissues. The 25 most common cross-tissue detection patterns are shown. For example, 1,229 proteins were detected and analyzed across all tissues and 1,003 proteins were detected and analyzed for only the spleen.
- (D) GO categories enriched in the 425 proteins detected and analyzed in only the three brain tissues.
- (E) Histograms of the proportion of variance explained by mouse, TMT tag, tissue/batch, and noise for the 1,229 proteins analyzed in all 10 tissues. Vertical dashed lines represent median proportions. Tissue and batch are confounded because all 20 samples for a tissue were measured across two tissue-specific batches. The gray square highlights proteins for which a large proportion of variation in abundance (5-95%) is explained by individual mouse ID.
- (F) Proteins with individual-specific abundance levels for all 20 mice, estimated as 95% prediction intervals from a random effects model. The 13 proteins for which mouse ID identity explained 5-95% of variation in protein abundance are shown.
- (G) The immunoglobulin IGHG2C had highly individual-specific abundance across the 10 tissues. Data are colored by sex and point shape corresponds to age.
- (H) GO categories enriched for in the 13 individual-specific proteins.

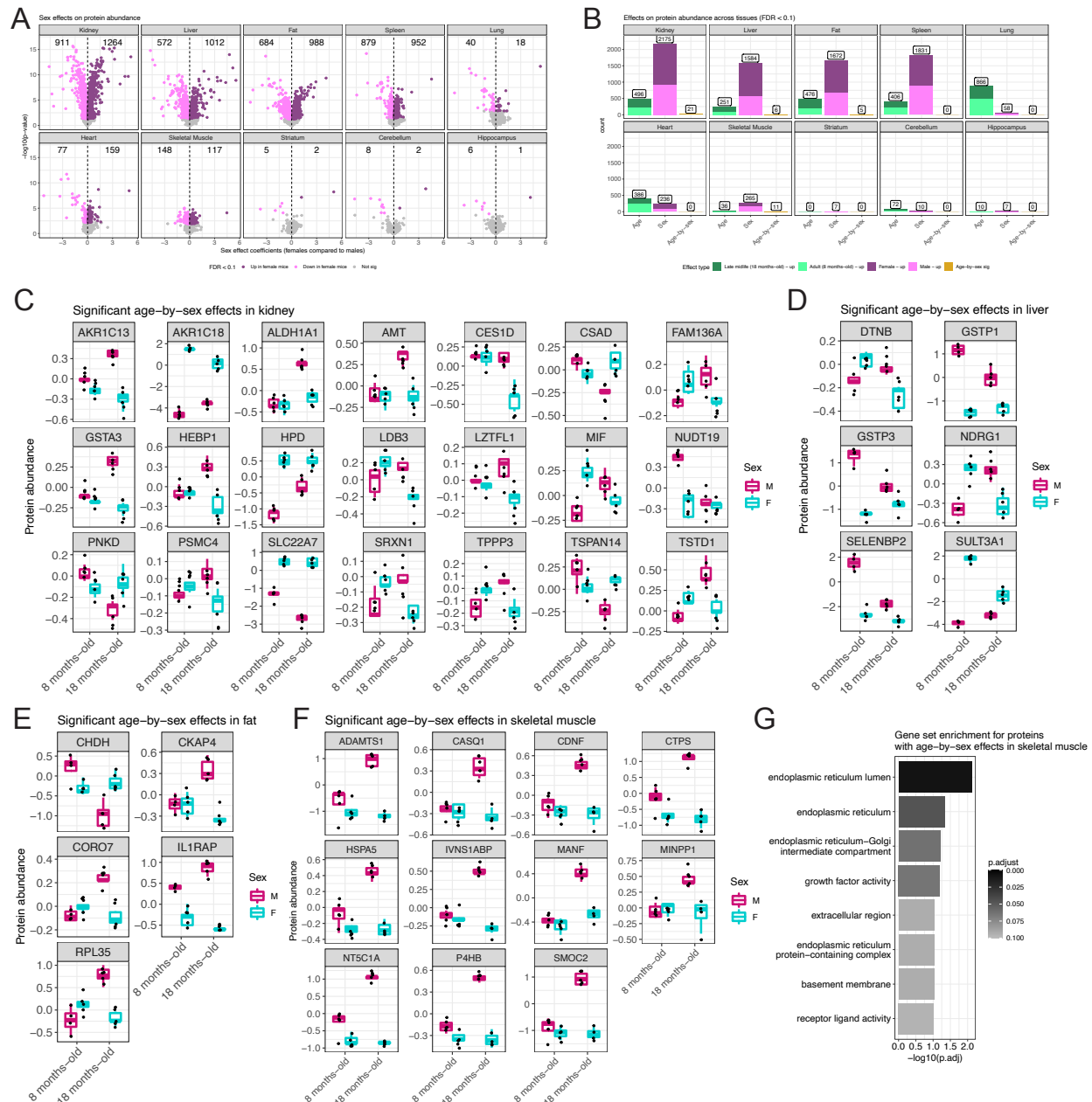


Figure S2. Proteins display age, sex, and age-by-sex differences in abundance. (A) Proteins with sex-related differences in abundance, across 10 tissues, represented as volcano plots. Differences in protein abundance are summarized as regression coefficients (x-axis) and corresponding $-\log_{10}(p\text{-value})$ (y-axis). Points are colored based on statistical significance (FDR < 0.1) and direction of effect. Counts of proteins with significantly higher abundance in females and males are included. Dashed vertical lines at 0 included for reference. Proteins with abundance age differences are shown in Figure 2. (B) Counts of proteins with age, sex, and age-by-sex differences (FDR < 0.1), across 10 tissues. Proteins with sex-by-age interaction effects (FDR < 0.1) in (C) kidney, (D) liver, (E) fat, and (F) skeletal muscle.

(E) Proteins with statistically significant GO categories enriched in proteins with age-by-sex interaction effects in skeletal muscle.

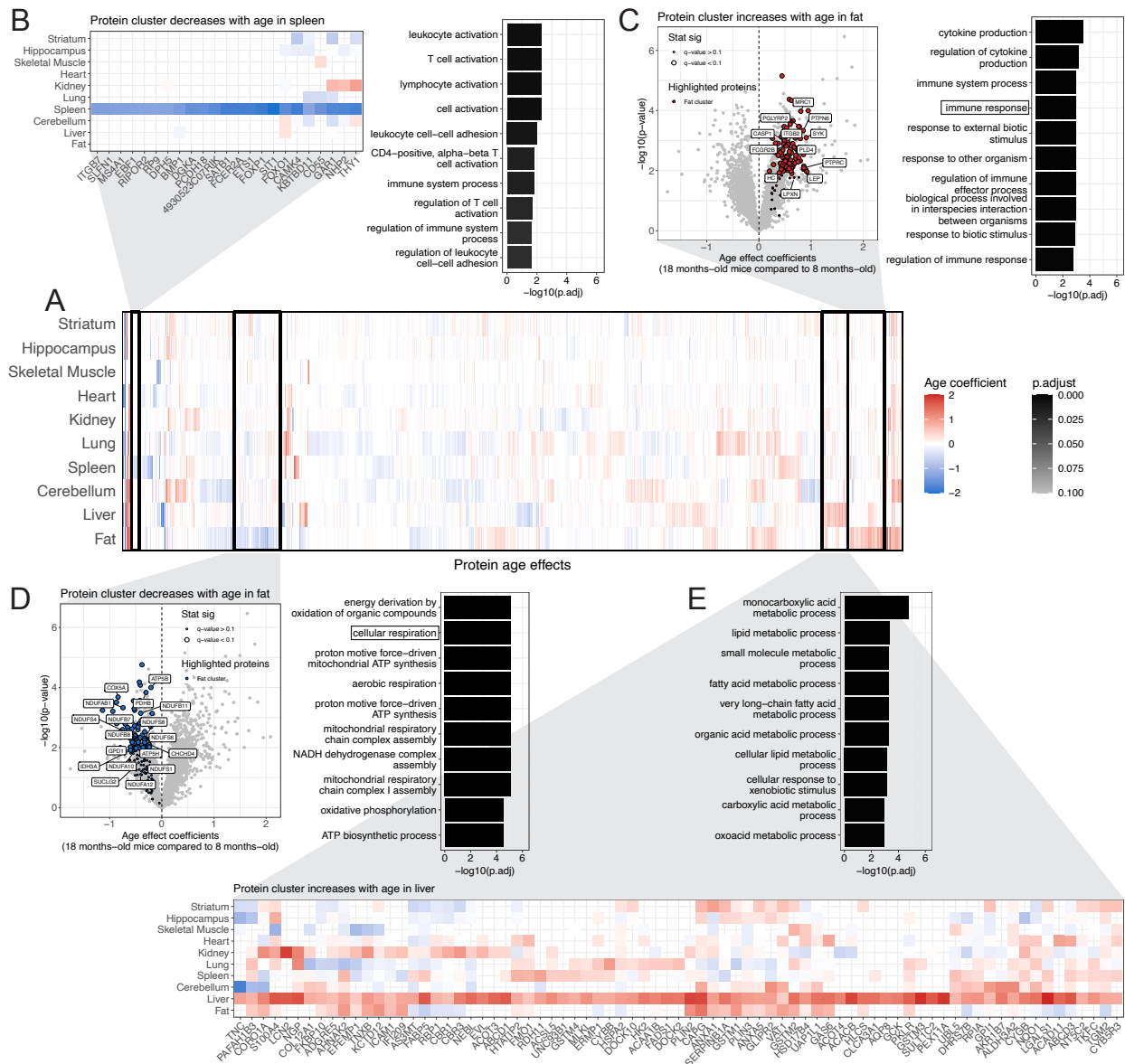


Figure S3. Additional patterns of aging unique to specific tissues.

(A) Age differences detected across the 10 tissues (FDR < 0.1), represented as a heatmap.

Differences are summarized as regression coefficients. Hierarchical clustering of the proteins (columns) reveals sets of proteins with age difference patterns that are unique to specific tissues.

Zoomed-in heatmaps are shown for (B) spleen-specific decreased abundance in proteins related to immune activation in older mice and (E) liver-specific increased abundance in proteins related to metabolic processes in older mice. Volcano plots are shown for (C) fat-specific increased abundance in proteins related to immune response and cytokine production in older mice and (D) fat-specific decreased abundance in proteins related to cellular respiration and the mitochondrial respiratory chain complex in older mice. Gene set enrichments are shown for all tissue-specific gene sets. Proteins from the immune response and cellular respiration GO categories (black boxes; GO:0045333 and GO:0006955, respectively) are highlighted in volcano plots for fat.

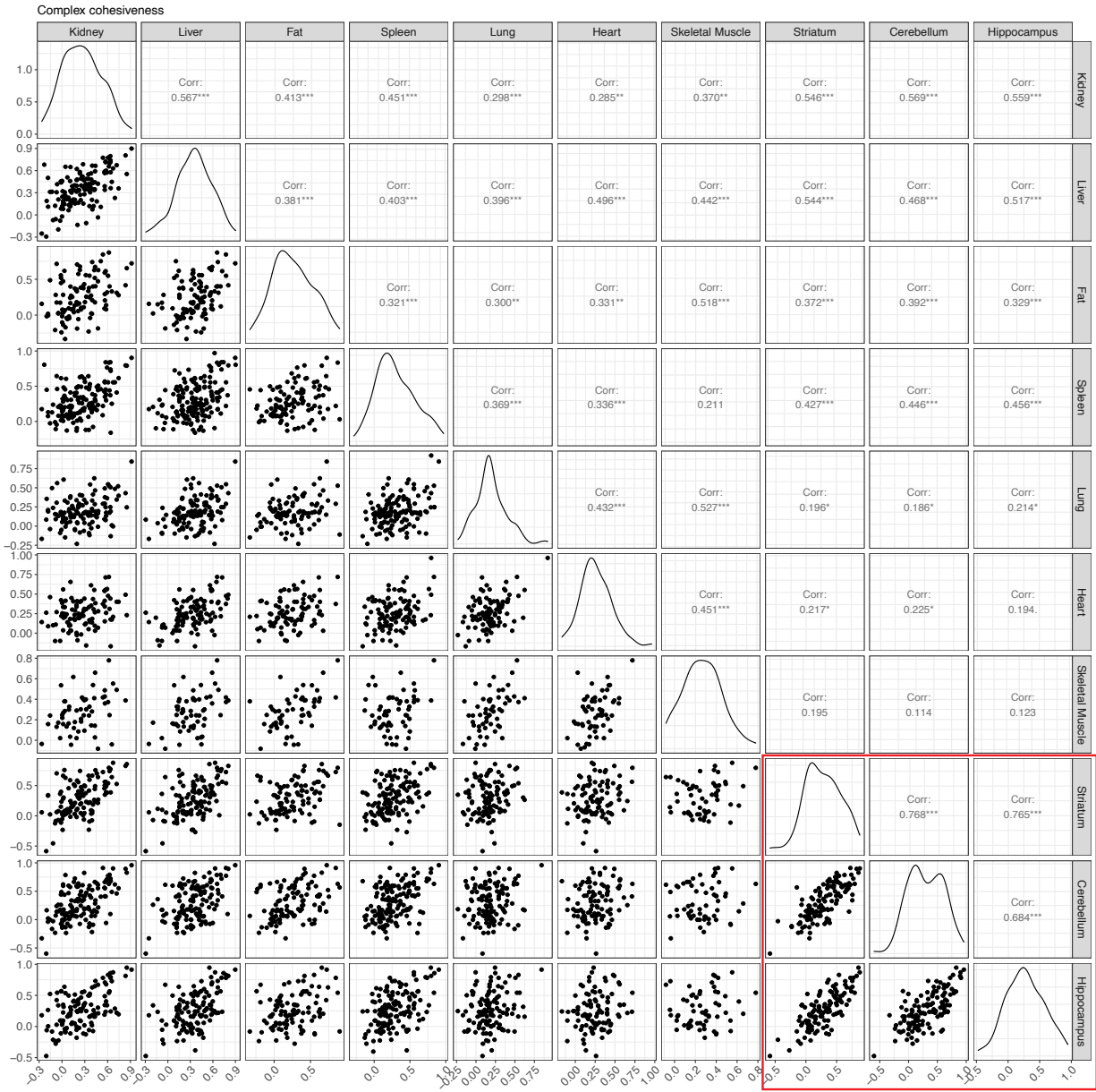


Figure S4. Comparison of protein complex cohesiveness between tissues.

Cohesiveness for protein complexes is summarized as the overall median across all median pairwise correlations for individual proteins with other complex members. The red square highlights the three brain tissues.

Protein complexes with (C) age-related and (D) sex-related differences in complex-wide correlation, represented as volcano plots. Differences in complex-wide correlations are summarized as the effect estimate from a paired *t*-test (x-axis) and corresponding $-\log_{10}(p\text{-value})$ (y-axis). Points are colored based on statistical significance ($\text{FDR} < 0.01$) and direction of effect. Dashed vertical lines at 0 included for reference.

Comparisons of $-\log_{10}(q\text{-values})$ for complex-wide abundance differences by complex-wide correlation differences due to (E) age and (F) sex. Vertical dashed line is included at 1 to denote significance for complex-wide abundance differences. Horizontal dashed line is included at 2 to denote significance for complex-wide correlation differences.

Comparison of the number of tissues that had a significant difference due to age (y-axis) and sex (x-axis), for (G) complex-wide abundance and (H) complex-wide correlation. Protein complex with significant differences in 2 or more tissues for both age and sex are labeled.

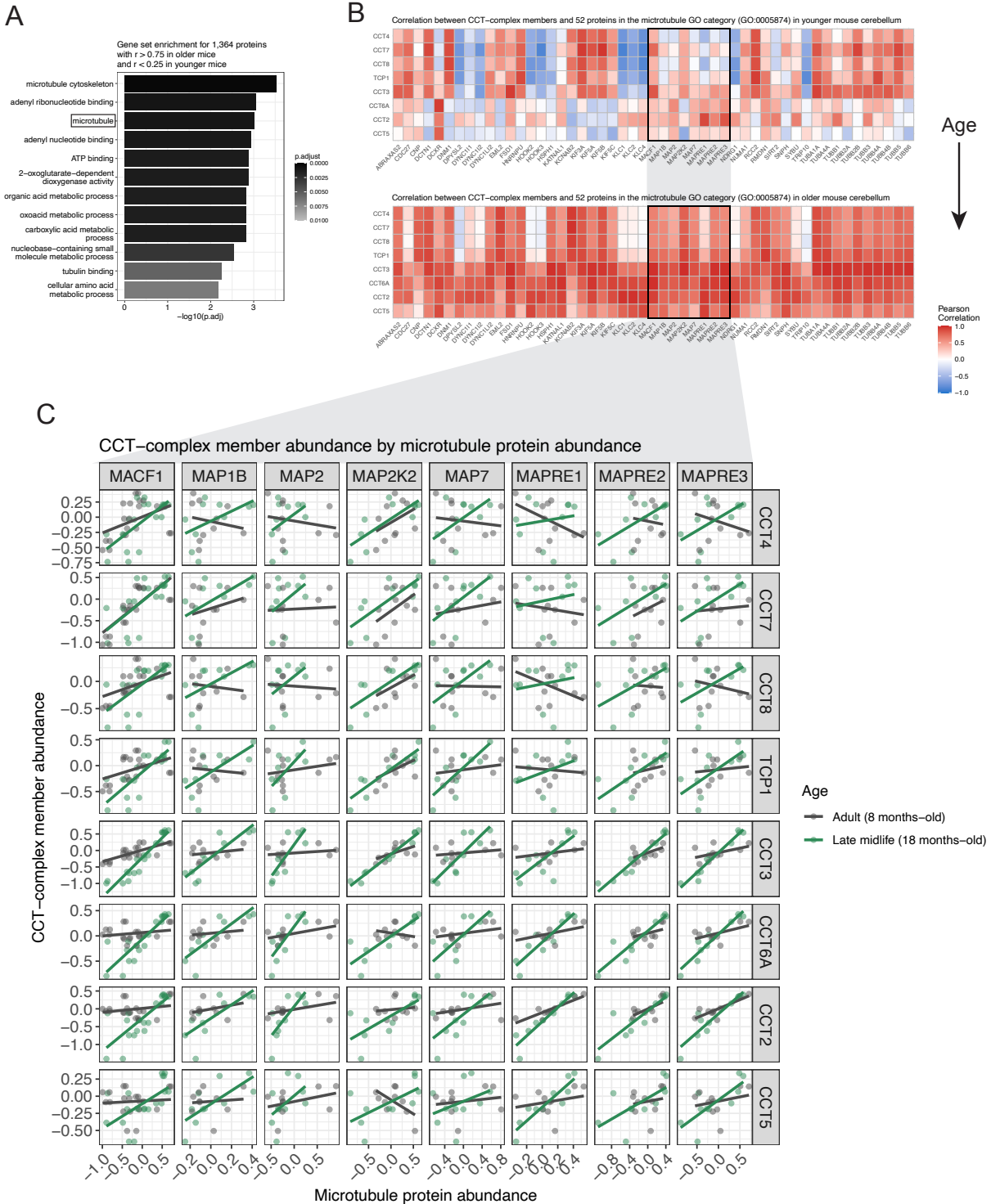
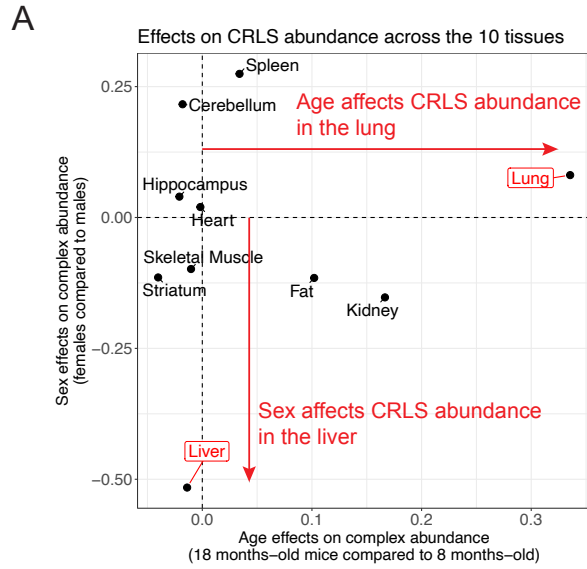


Figure S6. Microtubule proteins are more correlated with chaperonin-containing T-complex (CCT-complex) members in older mouse cerebellum.

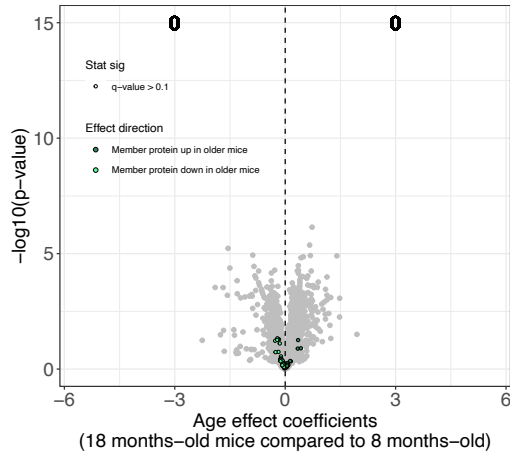
(A) GO categories enriched in proteins that are more correlated with CCT-complex members in older mouse cerebellum than younger. Proteins from the microtubule GO category (black box; GO:0005874) are highlighted.

(B) Pearson correlations between CCT-complex members and 52 microtubule proteins (GO:0005874) in younger (top) and older (bottom) mouse cerebellum. Black squares highlight eight microtubule-actin proteins.

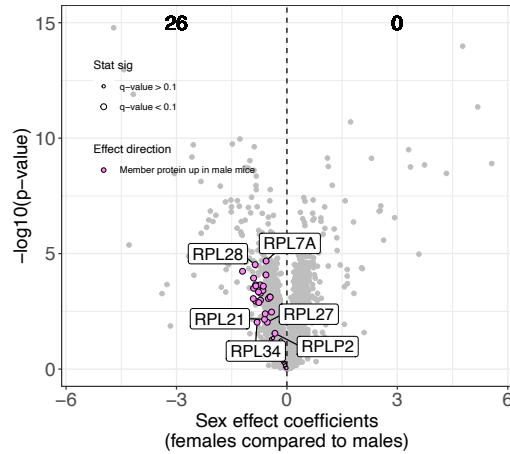
(C) Protein abundance of the eight CCT-complex members compared to the eight microtubule-actin proteins. Best fit lines included to reflect correlations. Points and lines are colored based on age.



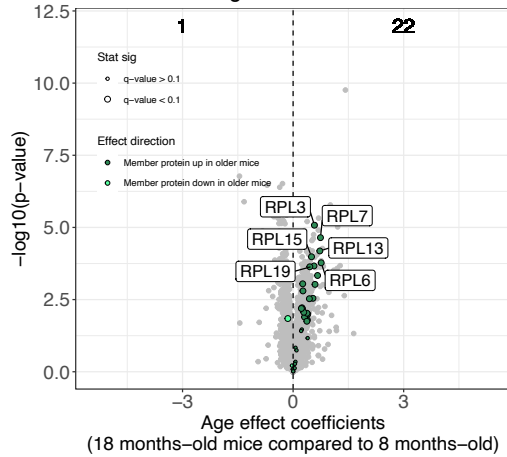
B Age effects on protein abundance of CRLS members in liver



Sex effects on protein abundance of CRLS members in liver



C Age effects on protein abundance of CRLS members in lung



Sex effects on protein abundance of CRLS members in lung

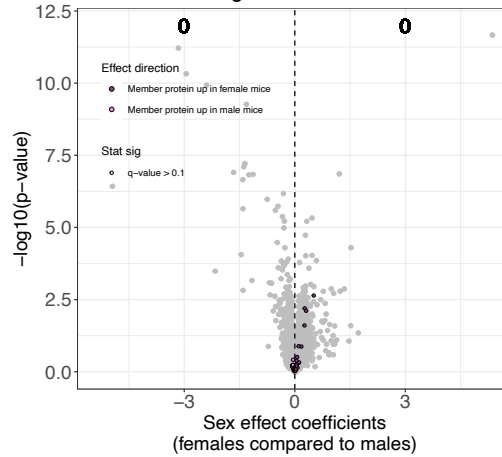


Figure S7. Complex-wide effects on the abundance of the cytoplasmic ribosomal large subunit (CRLS) differ between liver and lung.

(A) Comparison of age-related differences in complex-wide correlation (y-axis) to complex-wide abundance (x-axis) of the CRLS across the 10 tissues. Liver and Lung are highlighted in red.

(B) Age- (left) and sex-related (right) abundance differences for proteins in liver, represented as volcano plots. The x-axis is the (left) age or (right) sex effect coefficient and the y-axis is the corresponding $-\log_{10}(p\text{-value})$. CRLS members highlighted with color based on direction of effect. Counts of proteins with differences are included (FDR < 0.1).

(C) Age- (left) and sex-related (right) abundance differences for proteins in lung, represented as volcano plots. The x-axis is the (left) age or (right) sex effect coefficient and the y-axis is the corresponding $-\log_{10}(p\text{-value})$. CRLS members highlighted with color based on direction of effect. Counts of proteins with differences are included (FDR < 0.1).